Journal Name

ARTICLE TYPE

Multimodal quantification of degradation pathways during extreme fast charging of lithium-ion batteries: Electronic Supplementary Information

Eric J. McShane,[a*] Partha P. Paul,[b,c,d*] Tanvir R. Tanim,[e] Chuntian Cao,[f] Hans-Georg Steinrück,[g] Vivek Thampy,[b] Stephen E. Trask,[h] Alison R. Dunlop,[h] Andrew N. Jansen,[h] Eric J. Dufek,[e] Michael F. Toney,[i,j,‡] Johanna Nelson Weker,[b,‡] and Bryan D. McCloskey[a,‡]

S1   Cell Details

The graphite/nickel manganese cobalt oxide-532 ($LiNi_{0.5}Mn_{0.3}Co_{0.2}O_2$, NMC532) pouch cells used in this study were prepared at the Cell Analysis, Modeling, and Prototyping (CAMP) Facility at Argonne National Laboratory. The graphite electrode composition was 91.83 wt% Superior Graphite SLC1506T, 2 wt% Timcal C45 carbon, 6 wt% Kureha 9300 PVDF binder, 0.17 wt% oxalic acid, 9.94 mg/cm^2 total coating loading, 34.5% porosity, 70 μm coating thickness. The NMC532 electrode composition was 90 wt% Toda NMC532, 5 wt% Timcal C45 carbon, 5 wt% Solvay 5130 PVDF binder, 18.63 mg/cm^2 total coating loading, 34.5% porosity, 71 μm coating thickness. The dimensions and loadings of the electrodes are provided in Table S1. The electrolyte used was 1.2 M LiPF$_6$ in 3:7 by weight ethylene carbonate (EC) to ethyl methyl carbonate (EMC), and a Celgard 2320 (20 μm, polypropylene/polyethylene/polypropylene)

separator was used. Finally, an aluminized polymer material was used as the outer cover of the pouch cells.

Table S1 Relevant physical parameters for the NMC532 cathode and graphite anode used in this study.

Parameter	Cathode	Anode
Electrode area (cm^2)	14.1	14.9
Electrode thickness (μm)	71	70
Porosity (%)	35.4	34.5
Capacity (mAh)	37.6	44.7
Current Collector (CC)	Al	Cu
CC thickness (μm)	20	10
Total coating loading (mg/cm^2)	18.63	9.94
Single side coating density (g/cm^3)	2.62	1.42

[a] Chemical and Biomolecular Engineering, University of California & Energy Storage and Distributed Resources Division, Lawrence Berkeley National Laboratory, Berkeley, CA 94720, USA.

[b] SLAC National Accelerator Laboratory, 2575 Sand Hill Road, Menlo Park, CA 94025. USA.

[c] ESRF – The European Synchrotron, 71 Ave. des Martyrs, Grenoble, 38000. France.

[d] Henry Royce Institute, Department of Materials, The University of Manchester, Manchester, M1 3BB. UK.

[e] Energy Storage and Electric Transportation Department, Energy and Environmental Science and Technology, Idaho National Laboratory, Idaho Falls, ID 83415. USA.

[f] Computational Science Initiative, Brookhaven National Laboratory, Upton, NY 11973, USA.

[g] Department Chemie, Universität Paderborn, Warburger Str. 100, Paderborn, 33098. Germany.

[h] Chemical Sciences and Engineering Division, Argonne National Laboratory, 9700 South Cass Avenue, Lemont, IL 60439, USA.

[i] Department of Chemical and Biological Engineering, University of Colorado, Boulder, CO 80309, USA.

[j] Renewable and Sustainable Energy Institute (RASEI), University of Colorado, Boulder, CO 80309, USA.

* These authors contributed equally to this work.

‡ Corresponding authors; e-mails: michael.toney@colorado.edu, jlnelson@slac.stanford.edu, bmcclosk@berkeley.edu

S2 Formation Cycling and Fast Charge Capacity Losses

Table S2 lists the initial cell capacity, the capacity lost during formation cycling, the capacity lost during fast charge cycling, and the total capacity lost over formation and XFC cycling for each of the four cells examined in this study.

Table S2 Capacity Retention During Cycling for Four Tested Cells

Parameter	Cell 4C-a	Cell 6C-a	Cell 6C-b	Cell 6C-c
Initial Capacity (mAh)	41.25	42.08	42.30	40.38
Formation Capacity Loss (%)	12.61	16.80	15.92	12.14
XFC Capacity Loss (%)	7.09	22.49	19.69	20.38
Total Capacity Loss (%)	18.80	35.39	32.71	29.92

## S3 *Cell 6C-a*: Accounting for Partial Charge to 7.5% SOC

High energy X-ray diffraction (HEXRD) measurements were conducted on *Cell 6C-a* after 450 XFC cycles were completed. However, after HEXRD measurements but prior to shipping the cell to Berkeley for mass spectrometry titration (MST) measurements, the cell was charged to 7.5% SOC to alleviate safety risks associated with self-discharge and avoid Cu dissolution at low SOC during shipping. Thus, in order to directly compare HEXRD and MST measurements, we had to correct for the additional 7.5% lithiation of the graphite anode when it was titrated compared to when HEXRD measurements were performed. We assumed the additional 7.5% charge passed was uniformly distributed across the graphite electrode, which was confirmed to be a good assumption based on the uniform distribution of LiC_6 in the HEXRD map of the graphite electrode obtained after a full charge. We then subtracted this uniform amount of Li_xC_6 from each region in *Cell 6C-a* when comparing against HEXRD measurements. The error induced by this correction is likely to be small, as the amount of additional lithiated graphite present due to the partial charge was ~90 μmol (based on the added 7.5% SOC), compared to ~360 μmol of combined Li and Li_xC_6 measured via MST on the full electrode excluding the additional partial charge. Thus, instead of the typical 10% error (~36 μmol) for the MST-measured combined amount of Li and Li_xC_6, the error for *Cell 6C-a* was instead 12.5% (~45 μmol).

S4 Converting LLI Mechanisms and LAM$_{PE}$ to Corresponding Capacity Losses

S4.1 Irreversibly Plated Li

The amount of irreversibly plated Li was determined locally by integrating the Li HEXRD peak area and applying an appropriate baseline correction, as has been described in previous work[1].

The cumulative amount of plated Li and Li_xC_6 was also obtained via MST, but the amount of Li and Li_xC_6 cannot be quantified independently with MST. Nonetheless, the stoichiometry for the reaction of Li with H_2O to evolve H_2 gas upon titration is shown below. A comparison between HEXRD and MST measurements of the combined amounts of Li and Li_xC_6 are provided in Section S5.

$$Li + H_2O \longrightarrow LiOH + \frac{1}{2}H_2\uparrow \tag{S1}$$
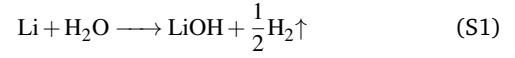
The amount of capacity lost due to dead plated Li was calculated by assuming Li was deposited via a one-electron process, as shown in Reaction S2 below.

$$Li^+ + e^- \longrightarrow Li \tag{S2}$$

The corresponding amount of capacity lost due to dead plated Li (Q_{lost}) was then calculated for a measured amount of dead plated Li (n_{Li}), as shown in Equation S3 below.

$$Q_{Li} = (n_{Li}) * \frac{1 \text{ mole e}^-}{\text{mole Li}} * \frac{96485 \text{ C}}{\text{mole e}^-} * \frac{\text{mAh}}{3.6 \text{ C}} \tag{S3}$$

S4.2 Dead Li_xC_6

The amount of dead Li_xC_6 was determined by integrating and summing the LiC_{12} and LiC_6 HEXRD peak areas. We note that more dilute phases of lithiated graphite, such as LiC_{30}, were only present in negligible quantities. The amount of dead Li_xC_6 which formed as a result of fast charge cycling was determined using the approach outlined in previous work[1].

The amount of capacity lost due to dead lithiated graphite (Li_xC_6) was calculated by assuming Li inserted into graphite via a "x" electron per Li_xC_6 process, as shown in Reaction S4 below.

$$xLi^+ + xe^- + C_6 \longrightarrow Li_xC_6 \tag{S4}$$
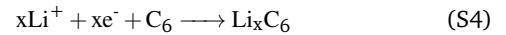
The corresponding amounts of capacity lost due to dead LiC_{12}, LiC_6, and Li_xC_6 were then calculated as shown below.

$$Q_{LiC6} = (n_{LiC6}) * \frac{1 \text{ mole e}^-}{\text{mole LiC}_6} * \frac{96485 \text{ C}}{\text{mole e}^-} * \frac{\text{mAh}}{3.6 \text{ C}} \tag{S5}$$

$$Q_{LiC12} = (n_{LiC12}) * \frac{0.5 \text{ mole e}^-}{\text{mole LiC}_{12}} * \frac{96485 \text{ C}}{\text{mole e}^-} * \frac{\text{mAh}}{3.6 \text{ C}} \tag{S6}$$

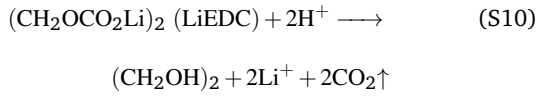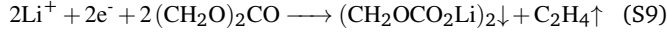$$Q_{LixC6} = Q_{LiC6} + Q_{LiC12} \tag{S7}$$

The cumulative amount of Li and Li_xC_6 was also measured via the amount of H_2 gas evolved upon titration, with reaction stoichiometry for LiC_6 shown below.

$$LiC_6 + H_2O \longrightarrow LiOH + C_6 + \frac{1}{2}H_2\uparrow \tag{S8}$$
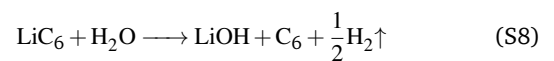
S4.3 Solid Carbonate Species

Several types of solid carbonate species, including lithium ethylene dicarbonate (LiEDC), lithium ethylene monocarbonate (LiEMC), and lithium carbonate (Li_2CO_3) have been observed in the graphite SEI formed under EC-containing electrolytes[2–5]. It is generally agreed that LiEDC deposits first via the reduction of EC, as shown in Reaction S9[3]. We note that LiEDC is a dicarbonate, so it evolves two CO_2 per LiEDC upon acid titration, as shown in Reaction S10. Thus, we treat a single LiEDC as two solid carbonate species.

$$2Li^+ + 2e^- + 2(CH_2O)_2CO \longrightarrow (CH_2OCO_2Li)_2\downarrow + C_2H_4\uparrow \quad (S9)$$

$$(CH_2OCO_2Li)_2 \ (LiEDC) + 2H^+ \longrightarrow \quad (S10)$$
$$(CH_2OH)_2 + 2Li^+ + 2CO_2\uparrow$$

However, LiEMC (instead of LiEDC) was recently discovered to be the predominant SEI species that persists on graphite electrodes after formation, and the authors proposed that LiEMC may form via a chemical reaction of LiEDC (likely with trace H_2O or H^+ impurities)[2]. The exact mechanism of formation, however, is not yet clear. With this in mind, we propose that LiEDC initially forms via a 2 e$^-$/LiEDC process, and then LiEDC chemically converts to LiEMC. We here note that LiEMC is a monocarbonate, and thus evolves one mole CO_2 per mole LiEMC upon acid titration, as shown in Reaction S11. For the purposes of the capacity loss calculation, we treat all solid carbonate species remaining on the graphite electrode after cycling as LiEMC, and each LiEMC corresponds to 2 e$^-$ worth of lost capacity (as the LiEDC-forming reaction originally required 2 e$^-$). Thus, the capacity lost due to solid carbonate deposition (Q_{carb}) is calculated using the moles of CO_2 evolved upon titration ($n_{CO2,titr}$) as shown in Equation S12 below.

$$HOCH_2CH_2OCO_2Li \ (LiEMC) + H^+ \longrightarrow \quad (S11)$$
$$(CH_2OH)_2 + Li^+ + CO_2\uparrow$$
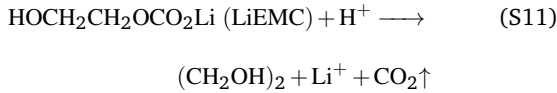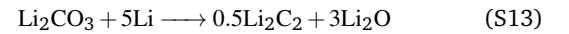
$$Q_{carb} = (n_{CO2,titr}) * \frac{2 \text{ mole e}^-}{\text{mole } CO_2} * \frac{96485 \text{ C}}{\text{mole e}^-} * \frac{mAh}{3.6 \text{ C}} \quad (S12)$$
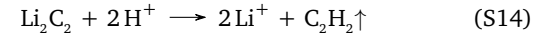
To decouple the amount of solid carbonates deposited during fast charge cycling from the solid carbonates deposited during initial formation cycling, we titrated a graphite electrode that had only undergone formation cycling, and we quantified 1.2 μmol/cm^2 solid carbonates on this electrode. We therefore determined the amount of solid carbonates deposited during fast charge cycling by subtracting 1.2 μmol/cm^2 solid carbonates from each region titrated.

S4.4 Li_2C_2

Li_2C_2 is hypothesized to predominantly form via the reaction of plated Li with existing solid carbonate species in the graphite SEI[6,7]. The exact mechanism of Li_2C_2 formation is not clear, but previous studies have shown that Li_2CO_3 can be reduced to form Li_2C_2, and it stands to reason the alkyl carbonates could also be reduced (or react with plated Li in a corrosion process) to form Li_2C_2 as well. Since Li_2C_2 contains 2 Li atoms that are no longer electrochemically active, we treat each Li_2C_2 as 2 e$^-$ worth of lost capacity (as 2 e$^-$ were used to plate the Li that ultimately reacted to form Li_2C_2). We consider this the minimum amount of capacity that could be lost due to Li_2C_2 formation, as the true mechanism of Li_2C_2 formation may involve additional species, such as the previously proposed[8] mechanism shown in Reaction S13.

$$Li_2CO_3 + 5Li \longrightarrow 0.5Li_2C_2 + 3Li_2O \quad (S13)$$

Li_2C_2 was quantified via the moles of C_2H_2 evolved upon titration, as shown in Reaction S14. The capacity lost due to Li_2C_2 formation (Q_{Li2C2}) is calculated using the moles of C_2H_2 evolved upon titration ($n_{C2H2,titr}$) as shown in Equation S15 below.

$$Li_2C_2 + 2H^+ \longrightarrow 2Li^+ + C_2H_2\uparrow \quad (S14)$$

$$Q_{Li2C2} = (n_{C2H2,titr}) * \frac{2 \text{ mole e}^-}{\text{mole } C_2H_2} * \frac{96485 \text{ C}}{\text{mole e}^-} * \frac{mAh}{3.6 \text{ C}} \quad (S15)$$

Similar to the solid carbonate calculation, to decouple the amount of Li_2C_2 deposited during fast charge cycling from the Li_2C_2 deposited during initial formation cycling, we titrated a graphite electrode that had only undergone formation cycling, and we quantified 37 nmol/cm^2 Li_2C_2 on this electrode. We therefore determined the amount of Li_2C_2 deposited during fast charge cycling by subtracting 37 nmol/cm^2 Li_2C_2 from each region titrated. The small amount of Li_2C_2 measured after formation cycling likely formed via a reaction involving solid carbonate SEI species directly in contact with lithiated graphite.

S4.5 LAM_{PE}

LAM_{PE} and LLI were both separately quantified using the dQ/dV fitting method described in the main manuscript. Simulated dQ/dV curves were manually adjusted to experimental data and LLI and LAM_{PE} values were extracted according to the method developed by Dubarry et al[9,10]. LLI generally manifests as a reduction in the ~3.6 V-centered peak area (compared to the peak area before fast charge cycling commences), and LAM_{PE} generally manifests as a reduction in the area of all dQ/dV peaks compared to the dQ/dV profile obtained before fast charge cycling. Simulated dQ/dV profiles were manually fitted until the root-mean-square error between experimental and simulated dQ/dV profiles was minimized, and LLI and LAM_{PE} values were determined from the resultant fitted curves. Representative dQ/dV curves at the end of XFC cycling (450th cycle) obtained through experiments

(solid curves) as well as the simulated curves (orange circles) for (a) *Cell 4C-a*, (b) *Cell 6C-a*, (c) *Cell 6C-b*, and (d) *Cell 6C-c* are shown in Figure S1. Although LLI was the major contributor to lost capacity in all four cells tested, the amount of LLI quantified via dQ/dV did not always exactly match the capacity lost during cycling. We attributed the small discrepancy between LLI and total capacity lost after the last XFC cycle (observed in main manuscript Figure 1) to capacity lost from LAM$_{PE}$. We note that it is possible for both LLI and LAM$_{PE}$ to contribute to capacity loss separately, depending on the extent of both aging modes and the heterogeneity within the cell[9].
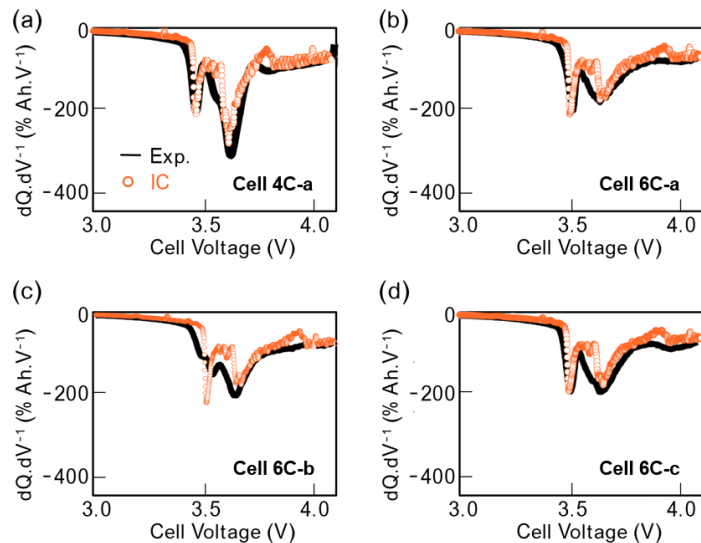

Fig. S1 Comparison between experimental (black, solid) and simulated (orange circles) dQ/dV curves at the end of the 450th XFC cycle for (a) *Cell 4C-a*, (b) *Cell 6C-a*, (c) *Cell 6C-b* and (d) *Cell 6C-c*.

S5 Comparison Between HEXRD and MST Measured Amounts of Dead Li and Dead Li$_x$C$_6$

The separate HEXRD and MST measurements of Li and Li$_x$C$_6$ can shed light on possible sources of uncertainty inherent to each measurement. As discussed in the main manuscript Section 2.4, one can reliably measure the combined amount ($\pm10\%$) of dead Li and Li$_x$C$_6$ with MST, but the amounts of Li and Li$_x$C$_6$ cannot be decoupled from one another. There is no known reason to expect the MST measurement to systematically underestimate or overestimate the true amount of Li and Li$_x$C$_6$, as the error arises primarily from the baseline correction of the evolved H$_2$ gas signal upon titration (about 5-10% of total). HEXRD has a key advantage over MST in that dead Li and Li$_x$C$_6$ can be separately measured. However, quantification is challenging with HEXRD for multiple reasons[1,11]. The crystalline peak of Li is relatively weak in intensity compared to other species in the cell and it lies on the shoulder of the much stronger NMC (cathode) peak, which makes its quantification challenging[12]. Li$_x$C$_6$ species (such as LiC$_6$ and LiC$_{12}$) are similarly challenging to quantify given the strong background signal from cell components. Additionally, not

all of the Li deposits may be large enough to be detectable above the HEXRD background from the pouch cell. With these limitations in mind, we find in Figure S2 that the HEXRD-measured combined amount of Li and Li$_x$C$_6$ (plotted for both the *global* cell scale and the *local* regions of *Cell 6C-a*) is ~80% of that measured by MST. This difference between HEXRD and MST measurements appears to be fairly agnostic of the charging protocol and region of a given cell. We note that the quantities plotted in Figure S2 below are the total amounts of Li and Li$_x$C$_6$ (including formation cycling), whereas the quantities plotted in the main manuscript include only Li and dead Li$_x$C$_6$ formed during XFC.
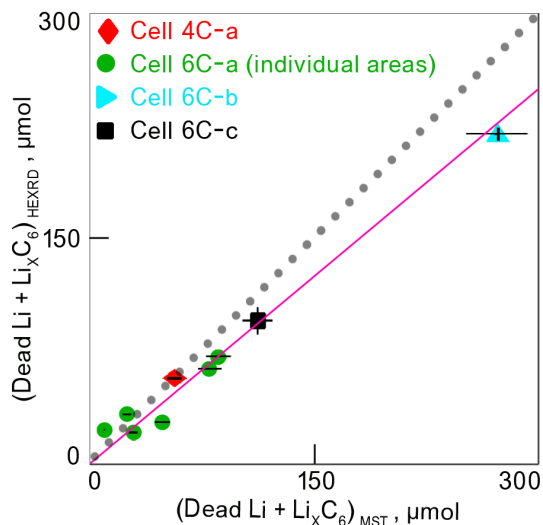
Fig. S2 Combined amount of Li and Li$_x$C$_6$ measured by HEXRD versus that measured by MST in each cell and in the different regions of *Cell 6C-a*. A gray dotted line of slope = 1.00 and y-intercept 0 is shown, affirming that the amount of Li and Li$_x$C$_6$ measured via HEXRD is generally less than that measured via MST. HEXRD detects ~80% of the total amount of plated Li and Li$_x$C$_6$, irrespective of the cell (shown by the pink line of slope = 0.80 and y-intercept 0 as a visual guide). The total amount of plated Li measured via HEXRD in each of these cells has also been reported in previous publications[1,13].

## S6 Correlating Cut Electrode Regions to HEXRD Pixels

Main manuscript Section 2.5 discusses combining MST and HEXRD in order to conduct a multimodal analysis on degradation pathways during XFC cycling. Figure S3 depicts a side-by-side comparison of HEXRD and MST maps for a representative cell (*Cell 6C-a*). The anode was cut into six regions, and each region was photographed separately prior to MST. The stitched image in Figure S3(a) was overlaid on the HEXRD map to obtain the corresponding HEXRD image in Figure S3(b), and MST and HEXRD measurements in specific regions (A-F) were used to uncover the *local* correlations between plated Li and other SEI species presented in main manuscript Figure 4.
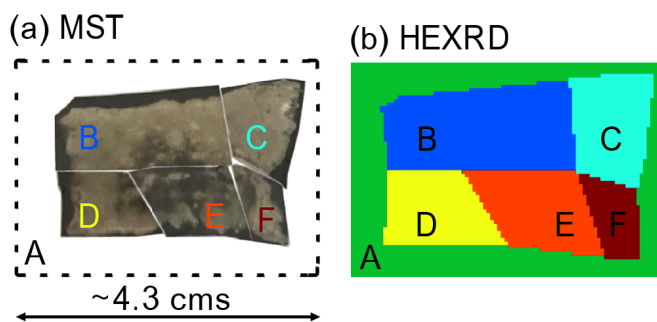
Fig. S3 Comparison between (a) optical images of cut electrode pieces used for MST measurements and (b) HEXRD map acquired for *Cell 6C-a*, with Regions A-F shown.

## S7 Global and Local Correlations Between Dead Li and Other Li-containing Species

Figure S4 shows the relationships between the amounts of various Li-containing species formed during XFC cycling and the amount of plated Li. This figure is a combination of the *global* (for each of the four cells) and *local* (for each individual area in *Cell 6C-a*) relationships shown in Figure 3 and Figure 4, respectively, in the main manuscript. As expected, the correlations between the amounts of each species and the amount of plated Li generally hold when viewed over the entire cell or over a smaller region of a cell with vastly different amounts of plated Li. Our analysis also emphasizes the larger scatter in the trends when viewed over smaller regions of a given cell (see scatter among red dots in Figure S4).
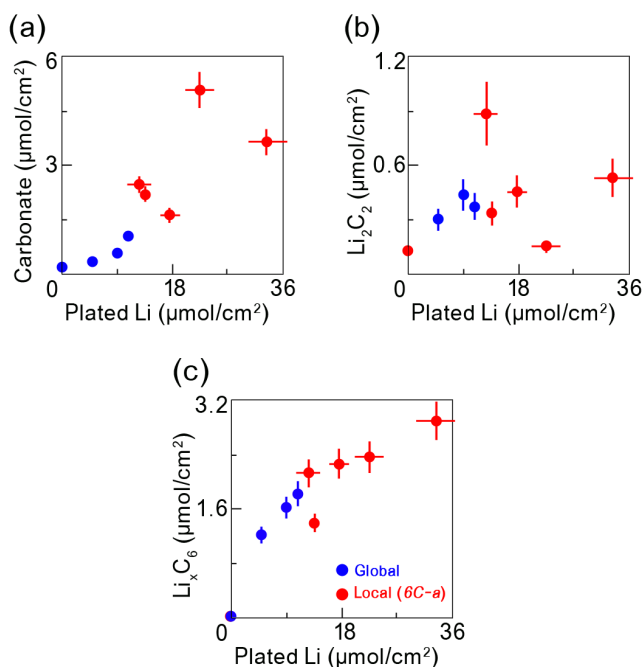
Fig. S4 Correlation between the amount of plated Li (in μmol/cm²) and amounts of (a) solid carbonate SEI species, (b) Li_2C_2, and (c) Li_xC_6. The plotted quantities encompass the four cells studied (blue dots), as well as the six regions (A-F) of *Cell 6c-a* (red dots).

S8 Additional Information Regarding *Cell 6C-c*

Main manuscript Section 3.3.2 discusses the effect of *local* LAM_{PE} on the *local* LLI in *Cell 6C-c*. In particular, at the bottom right corner of the cell, local cathode degradation is hypothesized to cause local LLI through the deposition of an unknown species on the anode. We postulate that there is no irreversibly plated Li in the bottom corner of the cell (despite the strong HEXRD signal shown in main manuscript Figure 5(c)) due to the absence of plated Li in the optical image in main manuscript Figure 5(b). Additionally, Figure S5(b) shows the HEXRD map of dead Li_xC_6 adjacent to the map of plated Li. Since plated Li is typically collocated with dead Li_xC_6 [13–15], and we do not observe a local abundance of LiC_6 in the cyan box region, this further supports our hypothesis that the region does not contain plated Li. Rather, some other species (possibly lithium oxyfluorophosphate based on the discussion in the main manuscript) is likely deposited on the anode.
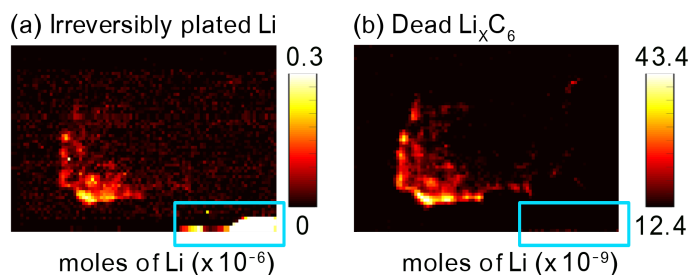
Fig. S5 HEXRD maps for the amount of (a) irreversibly plated Li and (b) dead Li_xC_6 for *Cell 6C-c*.

Notes and references

1 P. P. Paul, C. Cao, V. Thampy, H.-G. Steinrück, T. R. Tanim, A. R. Dunlop, E. J. Dufek, S. E. Trask, A. N. Jansen, J. N. Weker and M. F. Toney, *ACS Applied Energy Materials*, 2021.

2 L. Wang, A. Menakath, F. Han, Y. Wang, P. Y. Zavalij, K. J. Gaskell, O. Borodin, D. Iuga, S. P. Brown, C. Wang *et al.*, *Nature chemistry*, 2019, **11**, 789–796.

3 T. Liu, L. Lin, X. Bi, L. Tian, K. Yang, J. Liu, M. Li, Z. Chen, J. Lu, K. Amine *et al.*, *Nature nanotechnology*, 2019, **14**, 50–56.

4 A. M. Andersson, A. Henningson, H. Siegbahn, U. Jansson and K. Edström, *Journal of Power Sources*, 2003, **119**, 522–527.

5 P. Niehoff, S. Passerini and M. Winter, *Langmuir*, 2013, **29**, 5806–5816.

6 M.-T. Fonseca Rodrigues, V. A. Maroni, D. J. Gosztola, K. P. Yao, K. Kalaga, I. A. Shkrob and D. P. Abraham, *ACS Applied Energy Materials*, 2018, **2**, 873–881.

7 E. J. McShane, A. M. Colclasure, D. E. Brown, Z. M. Konz, K. Smith and B. D. McCloskey, *ACS Energy Letters*, 2020, **5**, 2045–2051.

8 N. Tian, C. Hua, Z. Wang and L. Chen, *Journal of Materials Chemistry A*, 2015, **3**, 14173–14177.

9 M. Dubarry, C. Truchot and B. Y. Liaw, *Journal of power sources*, 2012, **219**, 204–216.

10 T. R. Tanim, E. J. Dufek, M. Evans, C. Dickerson, A. N. Jansen, B. J. Polzin, A. R. Dunlop, S. E. Trask, R. Jackman, I. Bloom *et al.*, *Journal of The Electrochemical Society*, 2019, **166**, A1926.

11 H. Charalambous, O. J. Borkiewicz, A. M. Colclasure, Z. Yang, A. R. Dunlop, S. E. Trask, A. N. Jansen, I. D. Bloom, U. Ruett, K. M. Wiaderek *et al.*, *ACS Energy Letters*, 2021, **6**, 3725–3733.

12 H. Charalambous, D. P. Abraham, A. R. Dunlop, S. E. Trask, A. N. Jansen, T. R. Tanim, P. R. Chinnam, A. M. Colclasure, W. Xu, A. A. Yakovenko *et al.*, *Journal of Power Sources*, 2021, **507**, 230253.

13 P. P. Paul, V. Thampy, C. Cao, H.-G. Steinrück, T. R. Tanim, A. R. Dunlop, E. J. Dufek, S. E. Trask, A. N. Jansen, M. F. Toney, Weker and J. Nelson, *Energy & Environmental Science*, 2021, **14**, 4979–4988.

14 T. R. Tanim, P. P. Paul, V. Thampy, C. Cao, H.-G. Steinrück, J. N. Weker, M. F. Toney, E. J. Dufek, M. C. Evans, A. N. Jansen *et al.*, *Cell Reports Physical Science*, 2020, **1**, 100114.

15 D. P. Finegan, A. Quinn, D. S. Wragg, A. M. Colclasure, X. Lu, C. Tan, T. M. Heenan, R. Jervis, D. J. Brett, S. Das *et al.*, *Energy & Environmental Science*, 2020, **13**, 2570–2584.